Surface active oxygen engineering of photoanodes to boost photoelectrochemical water and alcohol oxidation coupled with hydrogen production

Yucong Miao [a], Zhenhua Li [a], Yingjie Song [a], Kui Fan [a], Jian Guo [a], Rengui Li [b], Mingfei Shao [a],*

[a] *State Key Laboratory of Chemical Resource Engineering, Beijing University of Chemical Technology, Beijing 100029, China*
[b] *State Key Laboratory of Catalysis, Dalian National Laboratory for Clean Energy, Dalian Institute of Chemical Physics, Chinese Academy of Sciences, Zhongshan Road 457, Dalian 116023, China*

ABSTRACT

Photoelectrochemical conversion of solar energy into fuels (or chemicals) is in urgent need of efficient photoanodes to drive its practical applications. Nevertheless, the development of high performance photoanode usually suffers from slow charge transfer and sluggish surface catalytic kinetics. Here, we report a surface active oxygen engineering strategy through the modification and activation of NiCo layered double hydroxide (NiCo-LDH), where the activated NiCo-LDH (NiCo-LDH-Act) captures the photogenerated holes and acts as cocatalyst for surface oxidation reactions. The as-developed $BiVO_4$/NiCo-LDH-Act achieves more than 3-fold higher photocurrent density than that of pristine $BiVO_4$. Experimental integrated with theoretical studies further testify the bifunctional of NiCo-LDH-Act for hole transport and catalytic reactions. Moreover, the adsorbed ·OH originated from active oxygen enables efficient oxidation of glycerol to attain 1,3-dihydroxyacetone (DHA) with a productivity of 20.5 μmol cm^{-2} h^{-1} at 1.4 V *vs.* RHE with simultaneously producing hydrogen at the cathode.

1. Introduction

Photoelectrochemical (PEC) water splitting offers a sustainable pathway to produce chemical fuels through solar energy, and efficient photoelectrodes have been always pursuing in the past few decades [1–3]. However, the most developed semiconductor-based photoanodes (such as $BiVO_4$, TiO_2, WO_3) usually suffers from slow charge transfer and sluggish surface catalytic kinetics, resulting in the easy recombination of photogenerated charges [4–6]. To improve the hole utilization efficiency, much efforts have been carried out such as introducing hole transfer layers and modifying cocatalysts [7–10]. For instance, Li et al. [11] developed a cooperative hole transfer layer (ferrihydrite) and Co_3O_4 cocatalyst to accelerate hole transport and surface water oxidation dynamics, thus enhance the PEC performance of Ta_3N_5 photoanode. Park et al. [12] inserted black phosphorene as a hole extraction layer between $BiVO_4$ and NiOOH to facilitates holes transfer. Although great progresses have been achieved, the stacking and integrating multiple functional layers on the photoanode always lead to unnecessary interfacial defect sites, which introduces new carrier recombination centers [13–16]. Accordingly, it is highly essential to design a simple bifunctional layer that can simultaneously realize fast charges transfer as well as efficient surface catalytic reactions.

For the purpose of maximize the hole utilization efficiency of photoelectrode, considering to apply appropriate reaction in PEC system to accelerate hole injection is significant. In the traditional PEC water splitting system, the photoanodic oxygen evolution reaction (OER) involves sluggish four-electron transfer processes, leading to a larger barrier to drive the overall water splitting compared to hydrogen evolution reaction (HER) at cathode [17]. In contrast, replacing OER with thermodynamically more favorable molecules oxidation provides a chance to fundamentally improve the efficiency of the PEC system, which not only effectively reduces the overpotential of hole-involved oxidation reactions on the photoanodes, but also has the benefits of upgrading cheap industrial feedstocks to high value-added products [18, 19]. Specifically, a variety of small molecule alcohols (e.g. methanol and benzyl alcohol) have been upgraded to aldehydes or acids [20,21], and the oxidation of biomass has also been studied, such as 5-hydroxymethylfurfural and glycerol [22,23]. Some hydrocarbons can be converted into alcohols or aldehydes by activation of C–H bonds in electrolytes containing organic solvents [24]. Recently, electrochemical

oxidation of alcohols is also of great interest due to the higher activity than OER as well as diversity of products [25–27]. Nevertheless, the frequent occurrence of C–C bond cleavage and peroxidation of hydroxyl groups in electrooxidation makes the selectivity hard to control, resulting in the product mostly tending to be low carbon number acid salts. Therefore, it is desirable but remains challenging to the selective oxidation of alcohols through the mild PEC process to produce higher value-added chemicals, thereby making the effective utilization of holes on the photoelectrode more meaningful.

Herein, we reported a surface active oxygen engineering strategy to simultaneously boost charges transfer and surface oxidation reactions of photoelectrodes, which guarantees the effective PEC oxidation of alcohols to high-value added chemicals coupled with efficient hydrogen generation (Scheme 1). Typically, the activated NiCo-layered double hydroxide (NiCo-LDH-Act) functional layer is modified on the $BiVO_4$ photoanode (denoted as $BiVO_4$/NiCo-LDH-Act), which achieves more than 3-fold photocurrent density enhancement than that of pristine $BiVO_4$ for PEC water oxidation. Experimental and spin-polarized density functional theory (DFT) studies reveal that the surface active oxygen formed by the oxidative dehydrogenation of hydroxyl groups on NiCo-LDH provides efficient active sites for hole capture and further oxidation reactions. Furthermore, the glycerol oxidation reaction based on $BiVO_4$/NiCo-LDH-Act photoanode is successfully achieved with a high photocurrent to 4.58 mA cm^{-2} at 1.23 V *vs.* RHE, capable of producing high-value-added 1,3-dihydroxyacetone (DHA) with a selectivity of 41.5% and a productivity of 20.5 µmol cm^{-2} h^{-1} at 1.4 V *vs.* RHE. Detailed radical recognition experiments confirmed that glycerol oxidation was mediated by adsorbed hydroxyl radicals evolved from the surface active oxygen of LDH.

2. Experimental section

### 2.1. Fabrication of $BiVO_4$/NiCo-LDH-Act photoanode

The preparation of the bismuth vanadate ($BiVO_4$) photoanode was conducted in accordance with a previously reported method [28]. The deposition of NiCo-LDH on the photoanode was performed in a three-electrode configuration with pristine semiconductor as working electrode, Pt wire and Ag/AgCl electrode as counter electrode and reference electrode, respectively. The electrolyte for the electrosynthesis of NiCo-LDH was obtained by dissolving $Co(NO_3)_2 \cdot 6H_2O$ (0.15 M) and $Ni(NO_3)_2 \cdot 6H_2O$ (0.15 M) in 20 mL of deionized water. The potentiostatic deposition was conducted at a potential of -1.0 V *vs.* Ag/AgCl, and the optimal loading amount of NiCo-LDH is 7.5×10^{-3} C. The semiconductor/NiCo-LDH-Act photoanode were then activated by cyclic voltammetry in 0.1 M KOH solution at a potential interval of 0–0.7 V for 3 cycles. The other cobalt based LDHs were synthesized and activated in the same way as NiCo-LDH except that $Ni(NO_3)_2 \cdot 6H_2O$ was changed to the corresponding metal salt solution. Specifically, ZnCo-LDH is synthesized in electrolyte containing $Co(NO_3)_2 \cdot 6H_2O$ and $Zn(NO_3)_2 \cdot 6H_2O$, while CoMn-LDH is electrodeposited in electrolyte dissolved with $Co(NO_3)_2 \cdot 6H_2O$ and $Mn(NO_3)_2$ solution (50 wt%).

2.2. Characterization

Characterization is detailed in Supplementary Information.

2.3. Photoelectrochemical measurements

The photoelectrochemical measurements were performed on electrochemical workstation (CHI 660E, CH Instruments) in a two-chamber quartz cell with a three-electrode configuration. The quartz cell is filled with 0.5 M Na_2SO_4 (pH = 7) electrolyte, and a nafion proton exchange membrane was utilization to separating anode chamber and cathode
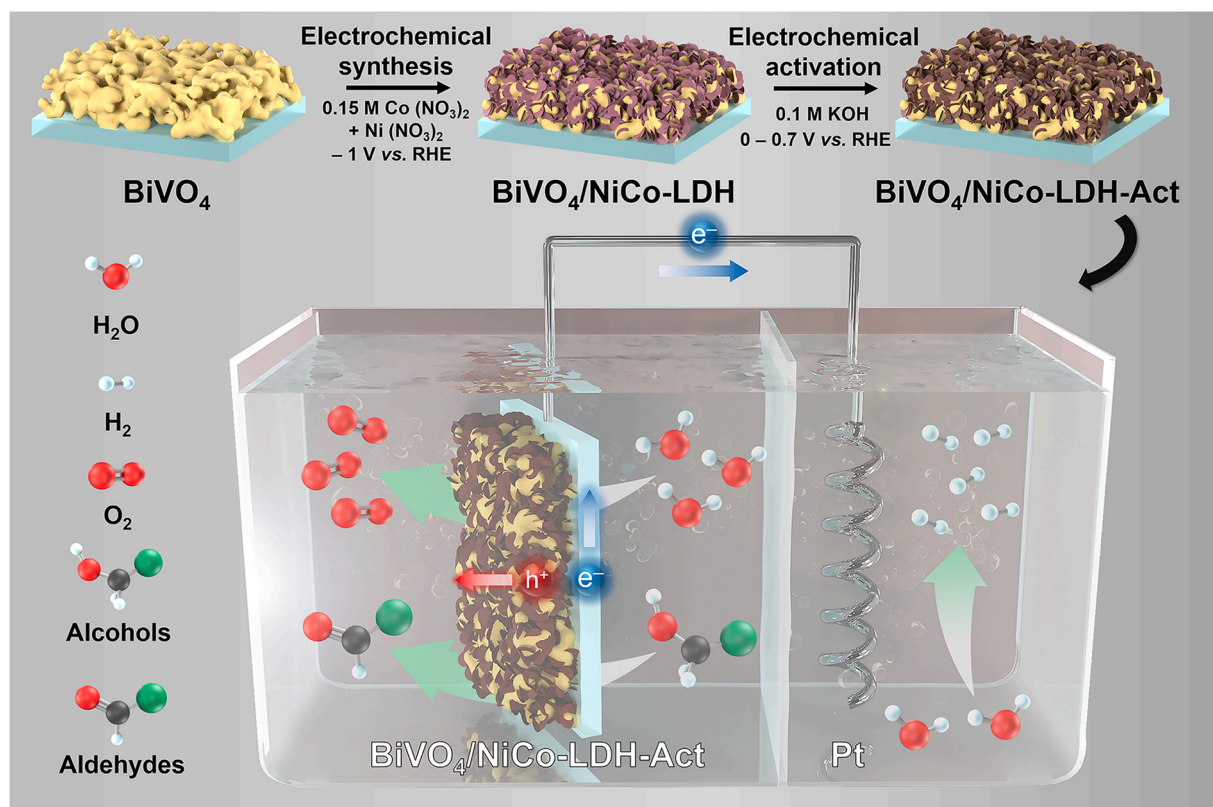
Scheme 1. Schematic diagram of sample preparation and photoelectrochemical system.

chamber. The working electrode and the Ag/AgCl reference electrode were configured in anode chamber, and the cathode cell is equipped with a Pt wire counter electrode. The light source used a 300 W Xe lamp equipped with an AM 1.5 G filter, and the irradiation power density was 100 mW cm^{-2}. The linear sweep voltammograms (LSV) were operated at 20 mV s^{-1} in a potential range from -0.4–1 V *vs.* Ag/AgCl. The measurement condition of transient photocurrent is the same as LSV, and the illumination or darkness is switched at a frequency of 3 s each time. Electrochemical impedance spectroscopy (EIS) was performed at 1.23 V *vs.* RHE with a frequency between 100 kHz and 1 Hz and 0.005 V amplitude of perturbation under illumination.

Other information about the experiment can be found in Supplementary Information.

3. Results and discussion

3.1. Synthesis and PEC performance of BiVO$_4$/NiCo-LDH-Act photoanode

The BiVO$_4$/NiCo-LDH-Act photoanode was synthesized by modifying a thin layer of NiCo-LDH on porous BiVO$_4$ followed by an activation process using electrochemical method in 0.1 M KOH electrolyte. As shown in Fig. 1a, XRD patterns of BiVO$_4$ growing on the FTO substrate correspond well to monoclinic scheelite BiVO$_4$ (JCPDS#14–0688), where the peaks at 18.7° and 28.8° can be designated as (110) and (−121) planes. After modification of NiCo-LDH as well as activation, the XRD pattern of the photoanode is almost unchanged, implying that the construction of this functional interface has no influence on the crystal structure of BiVO$_4$. The absence of peaks that assigned to LDH probably ascribes to the low mass loading of NiCo-LDH,

which can be verified by the appearance of NiCo-LDH characteristic peaks in the XRD pattern after further increasing the loading (Fig. S1). Scanning electron microscopy (SEM) images show typical nanosheet morphology of LDH that uniformly grown on the worm-like BiVO$_4$ particles (Fig. 1b). In addition, six small areas were selected from a wide area on the photoanode and magnified, and it can be observed that all BiVO$_4$ have uniform LDH growth from the SEM images (Fig. S2). Note that the size of the activated NiCo-LDH nanosheets is larger than its precursor (Fig. S3), possibly due to the continued growth of LDH in the alkaline solution. The photoanode structure observed by transmission electron microscopy (TEM) is consistent with the result of SEM (Fig. S4). Furthermore, the high-resolution TEM (HRTEM) image presents a core-shell structure with the BiVO$_4$ core wrapped by an NiCo-LDH-Act shell layer (Fig. 1c). The high-angle annular dark-field scanning transmission electron microscopy combined with energy dispersive spectroscopy (HAADF-STEM-EDS) mapping of BiVO$_4$/NiCo-LDH-Act indicates that the core elements of Bi and V combined with the outer shell layers of Ni and Co are uniformly distributed throughout the material (Figs. 1d and S5), further indicating the successful synthesis of BiVO$_4$/NiCo-LDH-Act. Additionally, using the similar method, we also introduced NiCo-LDH-Act on other typical photoanodes to fabricate TiO$_2$/NiCo-LDH-Act, WO$_3$/NiCo-LDH-Act and α-Fe$_2$O$_3$/NiCo-LDH-Act for comparison (Figs. S6–S8).

The PEC measurements were performed in 0.5 M Na$_2$SO$_4$ (pH = 7) electrolyte under AM 1.5 G illumination (100 mW cm^{-2}). The BiVO$_4$/NiCo-LDH-Act with different synthesis conditions were first optimized to obtain photoanodes with excellent performance (Supplementary Note 1). Consequently, the BiVO$_4$/NiCo-LDH-Act photoanode with optimal performances exhibits a photocurrent density of 3.29 mA cm^{-2} at 1.23 V *vs.* RHE in linear sweep voltammetry (LSV) measurement (Fig. 1e),
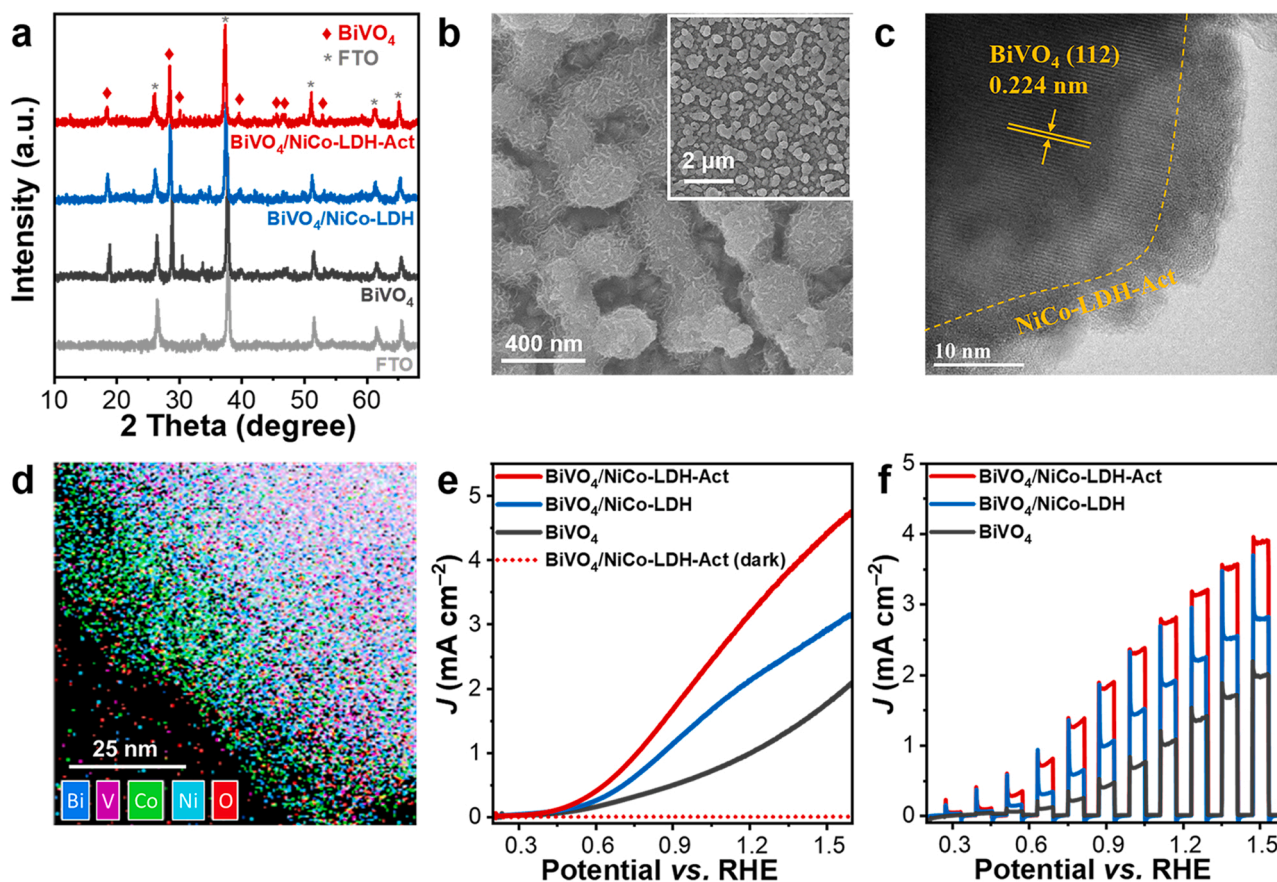

Fig. 1. (a) XRD diffraction patterns of FTO, BiVO$_4$, BiVO$_4$/NiCo-LDH, BiVO$_4$/NiCo-LDH-Act photoanodes. (b) SEM, (c) HRTEM images and (d) HADDF-STEM-EDS mapping of BiVO$_4$/NiCo-LDH-Act photoanodes. (e) LSV curves, (f) chopped current–potential curves of BiVO$_4$, BiVO$_4$/NiCo-LDH, and BiVO$_4$/NiCo-LDH-Act.

which is 3.13 and 1.49-folds higher compared to BiVO$_4$ and BiVO$_4$/NiCo-LDH (1.05 mA cm^{-2} and 2.20 mA cm^{-2}), respectively. Moreover, the as-prepared photoanodes was also studied by transient photocurrent measurements. All three photoanodes exhibit a rapid and reproducible photoresponse and current density in Fig. 1f, which are consistent with the LSV results (Fig. 1e). It is noteworthy that BiVO$_4$/NiCo-LDH without activation shows a prominent transient current spike and then reduces to a stable value, indicating the occurrence of electron-hole recombination [29]. This means that the modification of NiCo-LDH cocatalyst on BiVO$_4$ hampers hole migration, though it enables rapid surface reaction evidenced by the increased steady-state photocurrent. Encouragingly, the activation treatment of BiVO$_4$/NiCo-LDH slashed the spikes considerably to a constant high current density, demonstrating a bifunctionalities of NiCo-LDH-Act that can simultaneously improve the hole transfer and surface oxidation activity [20]. Moreover, the activation strategy can be extended to other metal oxide photoanodes, such as TiO$_2$, WO$_3$ and α-Fe$_2$O$_3$ (Figs. S6–S8). The PEC performance for these as-obtained semiconductors/NiCo-LDH-Act photoanodes demonstrates that the photocurrent density of each photoanode at 1.23 V *vs.* RHE is conspicuous increased by at least 1.4-fold (Figs. S11–S14), which confirms the extensive application of the developed strategy. In addition to NiCo-LDH-Act, transition metal hydroxides cocatalysts (e.g., Co(OH)$_x$, ZnCo-LDH, CoMn-LDH and CoFe-LDH) also shows much enhanced PEC activity by activation using electrooxidation strategy in alkaline electrolyte (Fig. S15).

3.2. Effect of activation process on NiCo-LDH

The above results clearly show that the activation of LDHs layer boost the PEC activity of photoanodes, so it is important to study the activation process in order to understand the mechanism of this interesting phenomenon. The measurement of electrochemical active area

found that the electrochemical areas of BiVO$_4$/NiCo-LDH-Act photoanode are increased slightly than that of pristine BiVO$_4$ (Fig. S16), which proves that the increase of micro surface area should not be the main reason for the performance improvement. X-ray photoelectron spectroscopy (XPS) is applied to demonstrate the changes of composition and elemental valence after activation of NiCo-LDH. The survey spectrum shows the presence of elements Bi, V, O, Co and Ni in BiVO$_4$/NiCo-LDH (Fig. S17). The high-resolution O 1 *s* XPS spectrum can be decomposed into three peaks located at 529.7 eV, 531.3 eV and 532.7 eV, which is attributed to O^{2-}, OH$^-$ and adsorbed oxygen species respectively (Fig. 2a) [30]. It is clear that the lattice oxygen content increased significantly after the activation treatment, which can be attributed to the dehydrogenation of the hydroxyl group, exposing the active oxygen on the LDH surface. In Fig. 2b, the Co 2$p_{3/2}$ peaks of BiVO$_4$/NiCo-LDH and BiVO$_4$/NiCo-LDH-Act at 780.5 eV, 782.7 eV and 786.6 eV are assigned to Co^{3+}, Co^{2+} and shake-up peaks, respectively [31]. Significantly, the peak area of trivalent cobalt shows an expansion after the activation treatment, meaning the oxidized state of Co. The Ni 2$p_{3/2}$ spectrum shows the characteristic peak at 855.6 eV and the satellite peak at 861.6 eV corresponding to divalent nickel, which maintains the same value during the activation process (Fig. 2c) [32]. This implies that the oxygen dehydrogenated on the hydroxyl group of NiCo-LDH is mainly exchanged electronically with the Co component. In addition, BiVO$_4$/Co(OH)$_x$ and BiVO$_4$/Ni(OH)$_x$ electrodes were prepared and the state of O elements during activation was monitored (Fig. S18). As a result, the lattice oxygen content of BiVO$_4$/Co(OH)$_x$-Act increases, while the O 1 *s* spectrum of BiVO$_4$/Ni(OH)$_x$-Act stays the same, further confirming the central role of Co metal in the activation process.

In-situ Raman spectra visualizes the reconfiguration process of the cocatalyst (Fig. 2d). The original peak of BiVO$_4$/NiCo-LDH located at 456 cm^{-1} is due to the A$_{1\,g}$ mode of Co(OH)$_x$ component in LDH. As the electrochemical activation proceeds, the Raman spectra signal of the
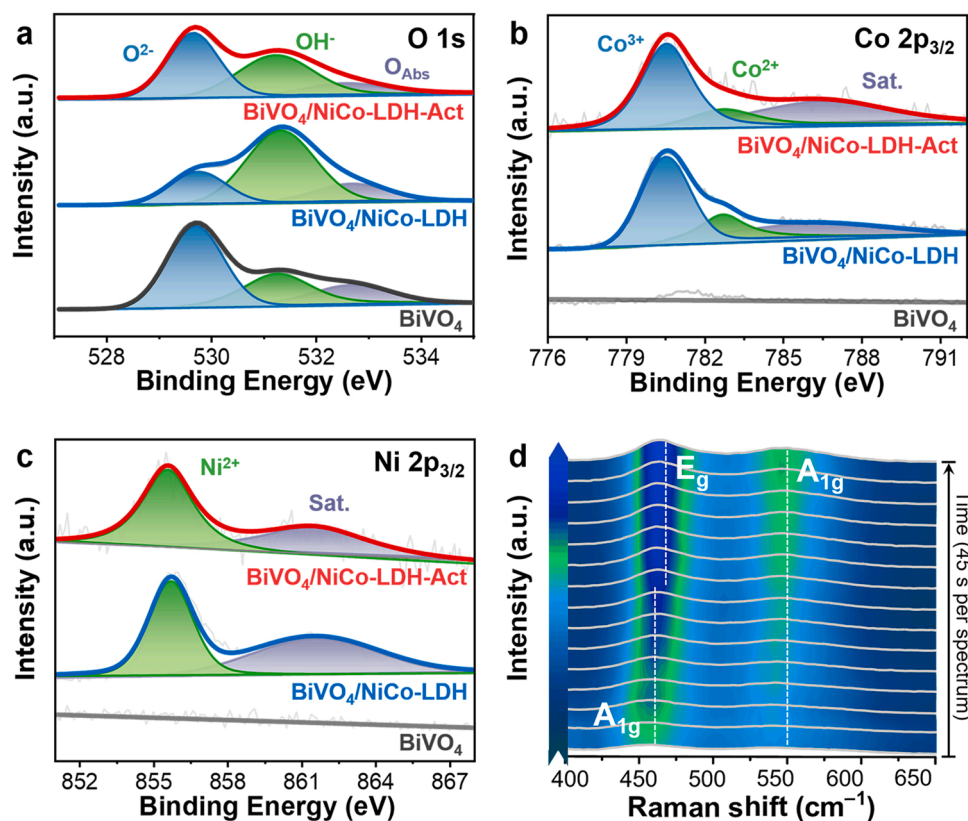

Fig. 2. High-resolution XPS spectra of (a) O 1 *s*, (b) Co 2$p_{3/2}$, and (c) Ni 2$p_{3/2}$ for BiVO$_4$, BiVO$_4$/NiCo-LDH, BiVO$_4$/NiCo-LDH-Act. (d) In-situ Raman spectra of the activation process of BiVO$_4$/NiCo-LDH photoanodes with a line interval of 45 s.

sample was tested every 45 s. Intriguingly, the peaks at 456 cm^{-1} vanished accompanied by the new peaks appearance at 465 cm^{-1} and 546 cm^{-1}, corresponding to the E$_g$ mode and A$_{1\,g}$ mode of CoOOH, respectively [33,34]. According to the results of this in-situ monitoring, it can be inferred that NiCo-LDH modified on the BiVO$_4$ is mainly increased the valence of cobalt during the activation process and the structure of Co(OH)$_x$ was transformed into CoOOH, but no change is detected for nickel, which was in accordance with XPS spectra results. In-situ Raman spectra of the activation process of BiVO$_4$/Co(OH)$_x$ and BiVO$_4$/Ni(OH)$_x$ electrodes were also conducted (Fig. S19). Variation of Raman spectra over time of BiVO$_4$/Co(OH)$_x$ is similar to that of BiVO$_4$/NiCo-LDH with a slight Raman shift. In contrast, the Raman signal of BiVO$_4$/Ni(OH)$_x$ sample shows an enhancement corresponding to the production of NiOOH at the beginning of the activation, but weakening at the later stage of activation due to the reduction of elemental Ni as a result of the negative scan polarity of the cyclic voltammetry. Subsequent resting diminished the signal to almost zero, suggesting that NiOOH is subject to spontaneous reduction in air due to instability. Therefore, the easily reducible NiOOH structure leads to the reconfiguration of NiCo-LDH to Ni(II)-doped Co(III)OOH structure instead of Ni(III)Co(III)OOH during the activation process. The above results indicate that BiVO$_4$/NiCo-LDH underwent structural

dehydrogenation during activation as expected, exposing a myriad of active oxygen sites.

3.3. Carrier behavior analysis

To shed light on the origin of the PEC performance enhancement by NiCo-LDH-Act, the behavior of photogenerated carriers was investigated. First, the charge injection efficiency and separation efficiency were calculated by adding a hole scavenger of Na$_2$SO$_3$ to the reaction system [35]. As shown in Fig. 3a, the surface active oxygen engineering by NiCo-LDH-Act increases the maximum charge separation efficiency of BiVO$_4$/NiCo-LDH-Act by 1.79 and 1.26-folds compared to the original BiVO$_4$ and BiVO$_4$/NiCo-LDH respectively. In addition, a maximum charge injection efficiency of 91.2% is achieved by BiVO$_4$/NiCo-LDH-Act (Fig. 3b), which is much higher than that of BiVO$_4$/NiCo-LDH (58.3%) and BiVO$_4$ (48.2%), implying the enhanced surface reaction kinetics by modifying activated NiCo-LDH. The electrochemical impedance spectroscopy (EIS) can also monitor surface reaction rates by evaluating the charge transport dynamics at the electrode/electrolyte interface. R_s and R_{ct} in the equivalent circuit fitting in Fig. 3c represent the series resistance and the surface charge transfer resistance, respectively [36]. The higher charge transfer resistance of pristine BiVO$_4$
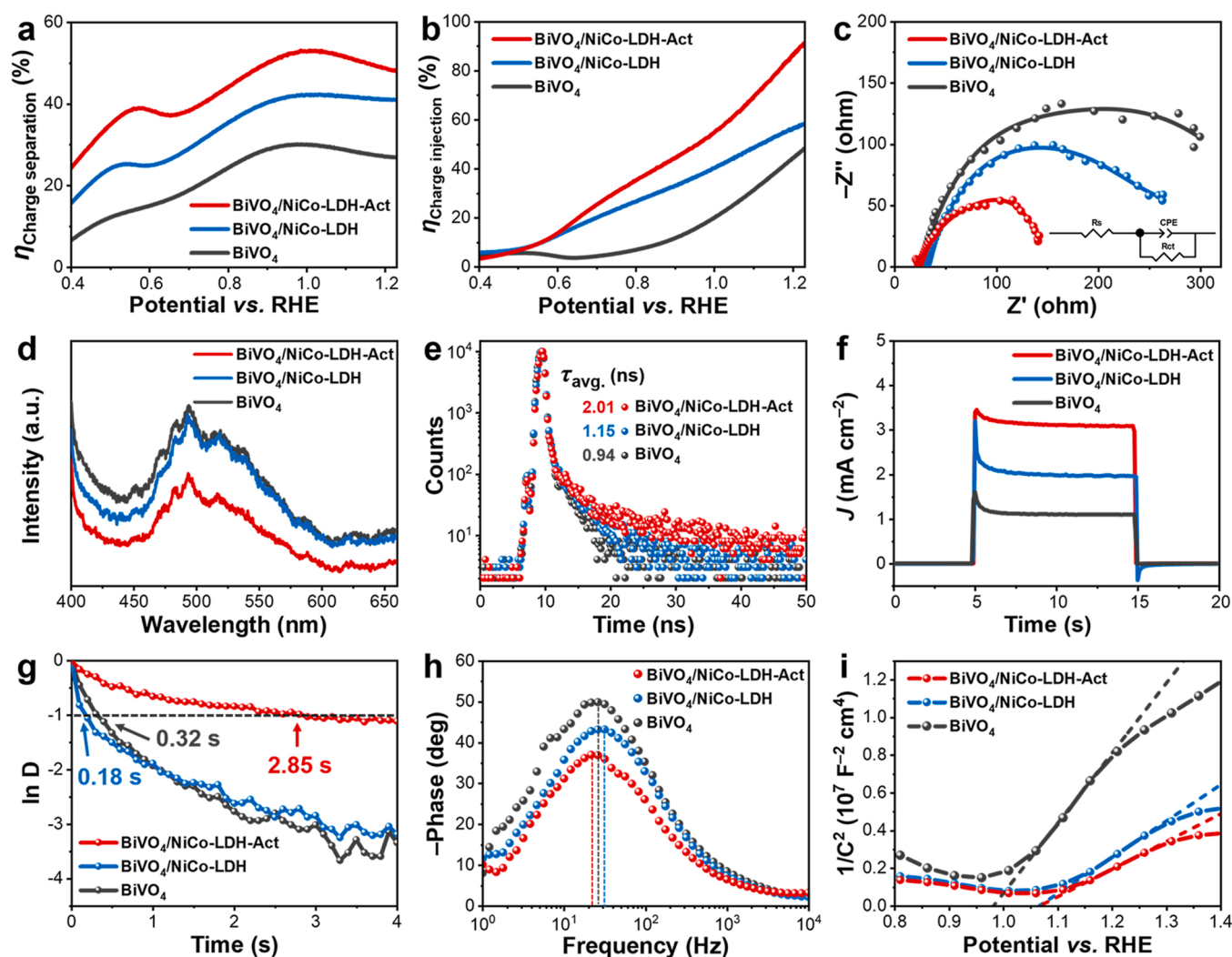

Fig. 3. (a) Charge separation efficiency, (b) charge injection efficiency, (c) EIS results (insert is equivalent circuit model) of BiVO$_4$, BiVO$_4$/NiCo-LDH, BiVO$_4$/NiCo-LDH-Act. (d) Steady-state PL spectra, (e) TRPL spectra (inset numbers are the average charge lifetime of each sample) of BiVO$_4$, BiVO$_4$/NiCo-LDH, BiVO$_4$/NiCo-LDH-Act. (f) Chopped chronoamperometry curves, (g) normalized transient current-time plots, (h) bode plots, (i) Mott-Schottky plots of BiVO$_4$, BiVO$_4$/NiCo-LDH, BiVO$_4$/NiCo-LDH-Act.

(331.5 Ω) was somewhat ameliorated by the deposition of NiCo-LDH (254.2 Ω), while the engineering of the surface activated oxygen greatly reduced migration resistance of surface holes (134.7 Ω).

Moreover, the recombination behavior of charges is studied by several electrochemical and optical tests. As shown in the steady-state photoluminescence spectroscopy (PL) (Fig. 3d), an emission peak elicited by an interband transition located at 500 nm can be observed in the three samples simultaneously. The lowest peak intensity of BiVO$_4$/NiCo-LDH-Act demonstrates its ability to attenuate the electron-hole recombination [37]. In Fig. 3e, time-resolved transient PL (TRPL) were performed to further analyze the photogenerated charge recombination kinetics, and fluorescence decay was fitted using the ExpDec2 model (the results are shown in Table S1) [38]. The average charge lifetimes ($\tau_{avg.}$) of BiVO$_4$, BiVO$_4$/NiCo-LDH, and BiVO$_4$/NiCo-LDH-Act

are 0.94 ns, 1.15 ns, and 2.01 ns, respectively, indicating that the effective utilization of holes in the photoanode leads to tardy charge recombination, thus showing prolonged lifetime.

The chopped chronoamperometry tests were performed and the results were normalized and integrated to investigate the charge mobility process in more depth. The transient spikes in Fig. 3f were normalized for quantification, and the transient photocurrent decay rate versus decay time (τ_D) was obtained (Fig. 3g) [39]. Surprisingly, the BiVO$_4$/-NiCo-LDH photoanode has even shorter τ_D than pristine BiVO$_4$ (0.18 s and 0.32 s) which implies extremely severe carrier recombination. Fortunately, the τ_D was dramatically extended to 2.85 s for BiVO$_4$/NiCo-LDH-Act. The electron lifetimes (τ_e) obtained by bode plots exhibit 70.53 ms, 5.03 ms and 6.09 ms for BiVO$_4$/NiCo-LDH-Act, BiVO$_4$/NiCo-LDH and BiVO$_4$, respectively (Fig. 3h) [39], further indicating the
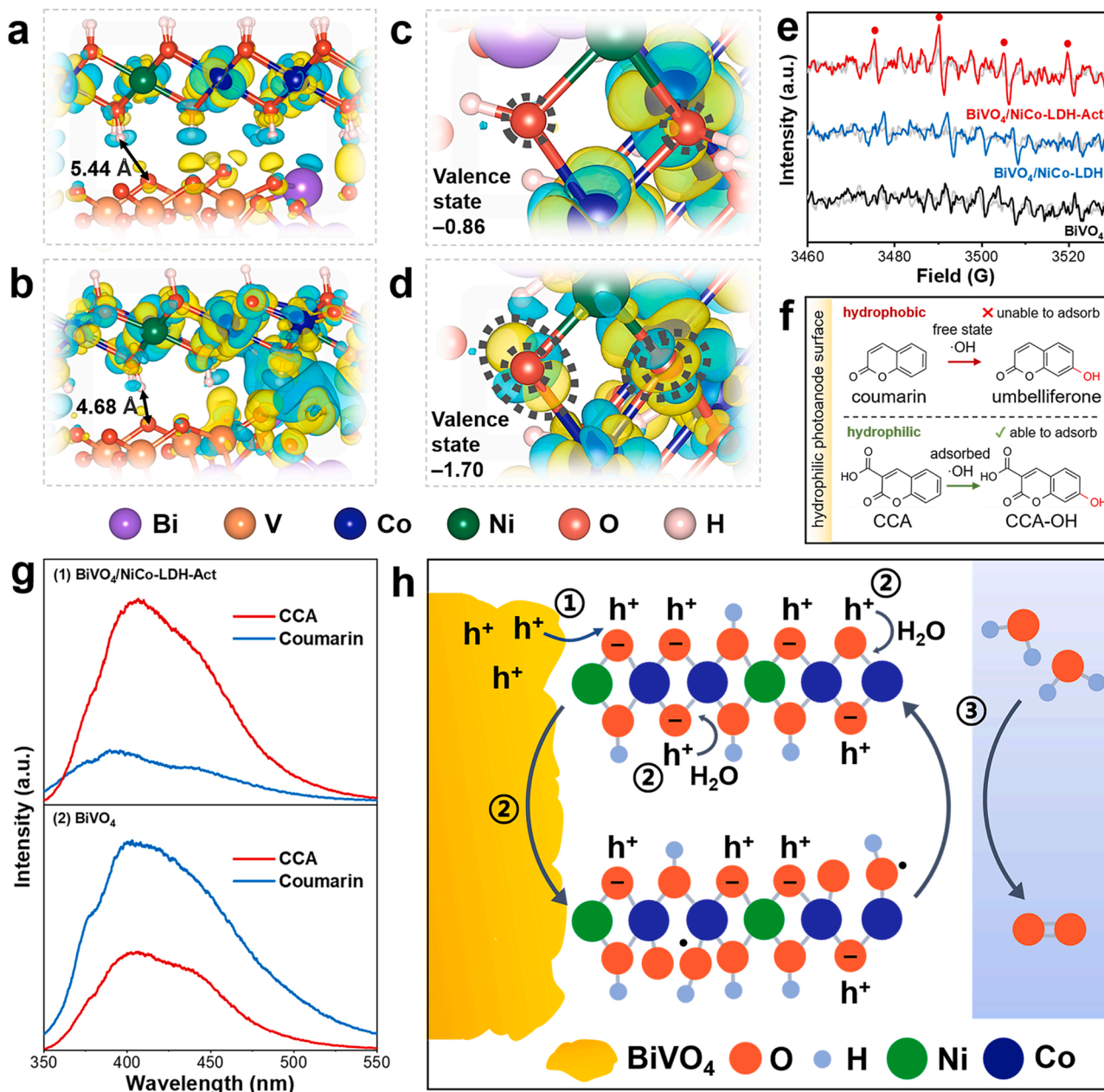

Fig. 4. Charge density difference maps between BiVO$_4$ and (a) NiCo-LDH, (b) NiCo-LDH-Act. Locally enlarged charge density difference maps (c) before and (d) after dehydrogenation of oxygen atoms on NiCo-LDH. The yellow and cyan regions represent electron accumulation and depletion, respectively. (e) EPR spectra of BiVO$_4$, BiVO$_4$/NiCo-LDH, BiVO$_4$/NiCo-LDH-Act, the light-colored line is the sample when it is not illuminated. (f) Formation of fluorescing molecules by the reaction of coumarin and CCA with ·OH radicals in different states. (g) PL spectra of ·OH capture results of coumarin and CCA on (1) BiVO$_4$/NiCo-LDH-Act and (2) BiVO$_4$ photoanode. (h) Schematic diagram of the generation and participation of adsorbed ·OH.

high charges separation efficient after modifying LDH-Act. In the Mott-Schottky measurement of Fig. 3i, the carrier density (N_d) of $BiVO_4$ photoanode can be calculated to be 5.59×10^{22} cm^{-3} from slope of the straight line in the curve, and the N_d of $BiVO_4$ increases to 1.08×10^{23} and 1.42×10^{23} cm^{-3} respectively after being influenced by modified NiCo-LDH and NiCo-LDH-Act. The increase in N_d reflects weakened carrier recombination. Moreover, the activation potential changes the N_d level in the sample (Fig. S22), which is exactly proportional to the photocurrent density of the sample (Fig. S10). These results all indicate that the $BiVO_4$/NiCo-LDH-Act promotes the holes migration at the semiconductor/cocatalyst interface and accelerates the surface reaction kinetics.

3.4. Discussion on active oxygen mechanism

To reveal the mechanism of surface active oxygen to PEC performances, density function theory (DFT) calculations were performed. The charge density difference maps before and after dehydrogenation of $BiVO_4$/NiCo-LDH visually show the transfer and accumulation of charges, and the Bader charge calculation quantifies the charge transfer [40]. As shown in Fig. 4a, the charge accumulation and depletion regions between $BiVO_4$ and NiCo-LDH have almost no crossover and overlap, which means that there is almost no charge transfer. In Fig. 4b, DFT calculations show that after the hydrogen atom on the hydroxyl group of NiCo-LDH is removed, the size and interaction degree of the electron cloud at the interface are obviously increased, implying the enhanced charge transfer between NiCo-LDH-Act and $BiVO_4$. The distance between the hydroxyl groups of LDH and the oxygen of $BiVO_4$ is shortened from 5.44 Å to 4.68 Å after activation, this phenomenon of tighter bonding at the semiconductor/cocatalyst interface further confirms the increased charge transfer between $BiVO_4$ and NiCo-LDH-Act. Focus on the details of the NiCo-LDH layer, it can be noticed that there is absence of electron transfer on the hydroxyl group, indicating that the interfacial transport of photogenerated holes is hindered (Fig. 4c). In comparison, the exposed active oxygen sites origin from the dehydrogenation of hydroxyl groups on NiCo-LDH-Act bear significantly more electron accumulation regions (Fig. 4d), thus inducing more holes from $BiVO_4$ to migrate to NiCo-LDH-Act. Further Bader charge calculation shows that the oxygen atoms on NiCo-LDH-Act layer show richer charge density than that of NiCo-LDH (7.69 and 7.18, respectively), which corresponds to the charge density difference results.

There are still doubts about how active oxygen species are participated in surface oxidation reactions. For this purpose, we monitored the state changes of active oxygen in the surface lattice during the reaction process by electron paramagnetic resonance (EPR) under illumination. 5,5-Dimethyl-1-pyrroline N-oxide (DMPO) was used as the spin-trapping agent, which is commonly used to trap ·OH radical species. As shown in Fig. 4e, $BiVO_4$ exhibits a weak EPR signal after irradiation. The generation of radicals was improved after modification of NiCo-LDH, and the characteristic EPR peaks of ·OH species could be observed [41]. The EPR spectrum of $BiVO_4$/NiCo-LDH-Act exhibited obvious signal of ·OH species, which tentatively demonstrated that surface active oxygen species would mainly participate in the reaction in the form of hydroxyl radicals.

It is well known that the detection of radicals by EPR focuses on the radicals in solution, so the weak hydroxyl radical signals indicate that probably most of the hydroxyl radicals are in the adsorbed state on the electrode surface. We therefore used a series of fluorescent probe molecular to inquire into the state of ·OH. Pure coumarin has no fluorescent properties, but the umbelliferone formed by grafting it with ·OH can emit strong fluorescent signal [42]. Since the hydrophobic coumarin is difficult to adsorb on the hydrophilic photoanode surface, it is employed here to judges the presence of free state ·OH. In contrast, the high polarity coumarin-3-carboxylic acid (CCA) can adsorb to the electrode surface and bind to the adsorbed state of ·OH to form 7-hydroxycoumarin-3-carboxylic acid (CCA-OH), then fluoresces to determine the

presence of adsorbed ·OH (Fig. 4f). As shown in Fig. S23, the fluorescence intensity of umbelliferone hardly decreased after homogeneously mixed with $BiVO_4$/NiCo-LDH-Act, while there was a significant decrease in peak intensity of CCA-OH, indicating that the division of labor between CCA and coumarin was reasonable. Afterwards, the CCA and coumarin molecules were introduced on the pristine $BiVO_4$ and $BiVO_4$/NiCo-LDH-Act respectively and then applied with continuous light. We found that $BiVO_4$/NiCo-LDH-Act makes the CCA molecules emitted a strong fluorescence signal while the fluorescence of coumarin is negligible, and the PL spectrum results of pristine $BiVO_4$ in the opposite, which reveal that $BiVO_4$/NiCo-LDH-Act has the majority of adsorbed radicals, while $BiVO_4$ yielded more free state radicals (Fig. 4g). The above results demonstrate that oxygen on the laminate is in-situ converted to adsorbed hydroxyl radicals after inducing holes to migrate onto it, then participate in the process of oxidation reaction (Fig. 4h).

3.5. PEC performance and mechanism of GOR

In addition to water oxidation, previous works have proven that hydroxyl radicals (especially adsorbed ·OH) can selectively upgrading of organic alcohols to valuable aldehyde/ketone products [43,44]. To maximize the utilization of adsorbed ·OH derived from surface active oxygen, we investigated the PEC performance of $BiVO_4$/NiCo-LDH-Act in alcohol oxidation. Glycerol oxidation reaction (GOR) was chosen as the model reaction on account of glycerol is an inexpensive feedstock ($0.66 per kg), which may give high added value products (such as $150 per kg of DHA) through catalytic oxidation [45]. The PEC glycerol oxidation reaction was performed in 0.5 M Na_2SO_4 (pH = 7) contained 0.6 M glycerol with $BiVO_4$/NiCo-LDH-Act photoanode. The LSV results in Fig. 5a show that the GOR exhibits a conspicuous increase in photocurrent density, reaching 4.58 mA cm^{-2} at 1.23 V *vs.* RHE, which was 1.39-fold than that of OER. Furthermore, chronoamperometry was used to study the distribution of GOR products under different bias, and the products were quantitatively analyzed by high performance liquid chromatography (HPLC). As shown in Fig. 5b, the PEC glycerol oxidation performance of $BiVO_4$/NiCo-LDH-Act gradually improved with rising potential, reaching a maximum of 41.93% DHA selectivity and 20.5 μmol cm^{-2} h^{-1} productivity at 1.4 V *vs.* RHE. The reason for the decrease in DHA selectivity with the further increasing bias may be due to the excessive oxidation of glycerol causes the break of C–C bond, which is manifested as an increase in the proportion of formic acid in the products. Compared with $BiVO_4$ and $BiVO_4$/NiCo-LDH, the DHA productivity of $BiVO_4$/NiCo-LDH-Act has a ~2-fold improvement (Fig. 5c). Surprisingly, the stability test of $BiVO_4$/NiCo-LDH-Act under AM 1.5 G (100 mW cm^{-2}) illumination maintains an appreciable photocurrent density after 70 h (Fig. S24), which is superior to the most reported $BiVO_4$ photoanodes. In addition, the extended alcohol substrates oxidation reaction has also been proved to enhance the performance of PEC system (Fig. S25). As shown in Table S2, benzyl alcohol and cyclohexanol were converted to benzaldehyde and cyclohexanone with a selectivity above 99%, respectively, and glucose was oxidized with a selectivity of 76.1% to obtain glyoxylic acid.

To investigate the mechanism of the GOR, several scavengers were added to the electrolyte to verify the main active species. Among them, Na_2SO_3 can act as a hole scavenger because its strong reduction performance is prior to other substrates being oxidized by holes, while *tert*-butanol is adopted as ·OH scavenger because it can consume ·OH to generate *tert*-butanol radicals stabilized by the hyperconjugation effect of alkyl. The results in Fig. 5d show the product cannot be detected after the hole is quenched by Na_2SO_3, indicating that photogenerated holes are the central driving force for glycerol oxidation. The addition of *tert*-butanol quenched ·OH also resulting in a sharp drop in the productivity of DHA, reflecting that ·OH can also mediates the selective conversion of glycerol to DHA. Furthermore, the core role of holes and ·OH is indirectly proved by the fact that the quenching of electrons and superoxide
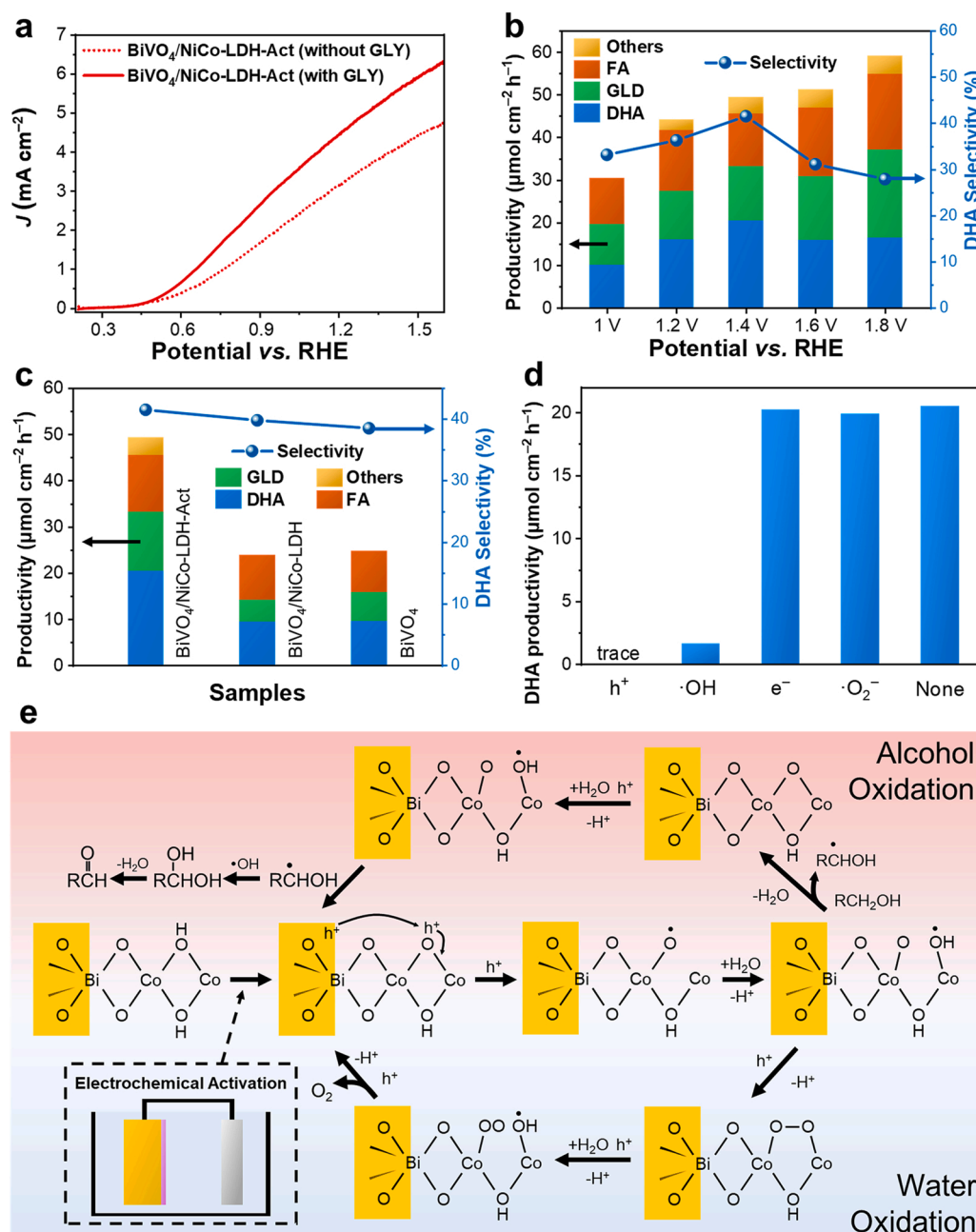
Fig. 5. (a) LSV curves of $BiVO_4$/NiCo-LDH-Act photoanode. (b) Productivity of organic products and DHA selectivity over $BiVO_4$/NiCo-LDH-Act photoanode at different potentials within 1 h. The products include DHA, glyceraldehyde (GLD), formic acid (FA) and others. (c) Productivity and DHA selectivity of organic products over $BiVO_4$, $BiVO_4$/NiCo-LDH and $BiVO_4$/NiCo-LDH-Act photoanodes at 1.4 V *vs.* RHE within 1 h. (d) DHA productivity in the presence of various radical scavenger (Na_2SO_3 for hole, *tert*-butanol for ·OH, $K_2S_2O_8$ for electron, and benzoquinone for ·O_2^-) at 1.4 V *vs.* RHE for 1 h. (e) Proposed mechanism of adsorbed ·OH mediated oxidation reaction.

radicals did not have much effect on the generation of DHA. From the above results, it can be speculated that the holes mainly contributed to oxidizing the exposed active oxygen on the photoanode surface to generate these ·OH, while a small number of holes also directly participate in the oxidation process of glycerol, which explains the phenomenon that the DHA does not completely disappear after quenching ·OH.

To further rationalize the hypothesis that adsorbed ·OH mediates glycerol oxidation, GOR was performed in 0.5 M $LiClO_4$ acetonitrile (MeCN) solution. As shown in the LSV curve of Fig. S26a, the $BiVO_4$/NiCo-LDH-Act photoanode exhibited lower photocurrent density in pure organic electrolyte than in aqueous electrolyte. Intriguingly, the photocurrent density was dramatically enhanced after adding glycerol to the organic electrolyte, and the increase was similar to that in the aqueous system, indicating that the GOR can also occur in the MeCN electrolyte. However, the analytical results of the organic products show that the DHA productivity and selectivity in organic electrolyte were only 3.5 µmol cm^{-2} h^{-1} and 20.8%, respectively, which were far lower

than the results in aqueous systems (Fig. S26b). This is due to the absence of H_2O in the organic electrolyte to supply adsorbed ·OH, verifying that adsorbed state ·OH is the major species driving the efficient and selective conversion of glycerol to DHA.

Based on the detail experiments and calculations, we propose the mechanism of PEC enhancement of $BiVO_4$/NiCo-LDH-Act (Fig. 5e). First, the surface of NiCo-LDH undergoes dehydrogenation reconstruction during the electrochemical activation process, and the valence of Co on the layer rises accompanied by the deprotonation of hydroxyl groups to expose surface active oxygen sites, which has been confirmed by XPS and in-situ Raman spectra in Fig. 2. According to our DFT calculation results, the negatively charged active oxygen on the surface of $BiVO_4$/NiCo-LDH-Act induce rapid migration of holes to surface catalysts, then the captured holes break the Co–O bond in-situ to construct active sites for accelerate the surface oxidation reaction kinetics. Subsequently, water molecules are grafted onto the photoanode surface and deprotonated to form a key intermediate adsorbed ·OH that identified by probe

molecules (see the PL spectra result in Fig. 4g). In the OER pathway, the rapid formation of adsorbed ·OH transition intermediate solves the key initial steps for the smooth progress of the four-charges OER process. After the completion of the remaining three steps, the surface of the photoelectrode is restored to the activated state to complete a cycle. The path is varied in alcohol oxidation, radical quenching experiments (Fig. 5d) proves that the adsorbed ·OH directly acts as the oxidant, which can selectively and efficiently dehydrogenate alcohols to the corresponding aldehydes. Finally, after the formation and utilization of adsorbed ·OH twice, the two-charges alcohol oxidation reaction is realized.

4. Conclusion

In conclusion, the surface active oxygen engineering on photoanode by a facile modification and activation of LDH achieves the dual purpose of promoting hole transfer and accelerating the surface oxidation reaction kinetics. Furthermore, we have realized the efficient photoelectrochemical high value-added organics production coupled with hydrogen generation system, implying the efficient utilization of overall photogenerated charge. The surface active oxygen strategy is applicable to a variety of cobalt-based LDH and metal oxide semiconductors, among which the combination of $BiVO_4$/NiCo-LDH-Act photoanode achieves a 3.13-fold increase in photocurrent density (3.29 mA cm^{-2} at 1.23 V *vs.* RHE) compared to pristine $BiVO_4$. XPS, in-situ Raman spectra and spin-polarized density functional theory (DFT) studies reveal that the conspicuous performance originates from the exposure of active oxygen sites after dehydrogenation of NiCo-LDH, which can induce the rapid migration of photogenerated holes due to its negatively charged characteristic and capture holes to catalyze surface reactions. The as-prepared photoanode also has impressive performance for GOR to obtain DHA with high selectivity and stability. EPR and fluorescent probe molecular experiments identified that the adsorbed hydroxyl radicals produced by in-situ oxidation of surface active oxygen mediates the efficient selective oxidation of glycerol. The development of this surface active oxygen engineering strategy on photoanodes and in-depth understanding of the mechanism will give a strong impetus to the promising topic of photoelectrochemical oxidation.

CRediT authorship contribution statement

Yucong Miao: Investigation, Methodology, Validation, Visualization, Writing – original draft. **Zhenhua Li:** Methodology, Supervision, Writing – review & editing. **Yingjie Song:** Methodology, Validation. **Kui Fan:** Methodology, Validation. **Jian Guo:** Supervision, Writing – review & editing. **Rengui Li:** Supervision, Writing – review & editing. **Mingfei Shao:** Conceptualization, Supervision, Funding acquisition, Project administration, Writing – review & editing.

Declaration of Competing Interest

The authors declare that they have no known competing financial interests or personal relationships that could have appeared to influence the work reported in this paper.

Data availability

Data will be made available on request.

Acknowledgement

Appendix A. Supporting information

References

[1] S. Wang, G. Liu, L. Wang, Crystal facet engineering of photoelectrodes for photoelectrochemical water splitting, Chem. Rev. 119 (2019) 5192–5247, https://doi.org/10.1021/acs.chemrev.8b00584.

[2] S. Ye, W. Shi, Y. Liu, D. Li, H. Yin, H. Chi, Y. Luo, N. Ta, F. Fan, X. Wang, C. Li, Unassisted photoelectrochemical cell with multimediator modulation for solar water splitting exceeding 4% solar-to-hydrogen efficiency, J. Am. Chem. Soc. 143 (2021) 12499–12508, https://doi.org/10.1021/jacs.1c00802.

[3] Y. Zhang, H. Lv, Z. Zhang, L. Wang, X. Wu, H. Xu, Stable unbiased photo-electrochemical overall water splitting exceeding 3% efficiency via covalent triazine framework/metal oxide hybrid photoelectrodes, Adv. Mater. 33 (2021) 2008264, https://doi.org/10.1002/adma.202008264.

[4] R. Gao, S. Liu, X. Guo, R. Zhang, J. He, X. Liu, T. Nakajima, X. Zhang, L. Wang, Pt-induced defects curing on BiVO4 photoanodes for near-threshold charge separation, Adv. Energy Mater. 11 (2021) 2102384, https://doi.org/10.1002/aenm.202102384.

[5] F. Ning, M. Shao, S. Xu, Y. Fu, R. Zhang, M. Wei, D.G. Evans, X. Duan, TiO2/graphene/NiFe-layered double hydroxide nanorod array photoanodes for efficiet photoelectrochemical water splitting, Energy Environ. Sci. 9 (2016) 2633–2643, https://doi.org/10.1039/c6ee01092j.

[6] W. Jiang, Y. An, Z. Wang, M. Wang, X. Bao, L. Zheng, H. Cheng, P. Wang, Y. Liu, Z. Zheng, Y. Dai, B. Huang, Stress-induced BiVO4 photoanode for enhanced photoelectrochemical performance, Appl. Catal. B Environ. 304 (2022), 121012, https://doi.org/10.1016/j.apcatb.2021.121012.

[7] W. Yang, R.R. Prabhakar, J. Tan, S.D. Tilley, J. Moon, Strategies for enhancing the photocurrent, photovoltage, and stability of photoelectrodes for photoelectrochemical water splitting, Chem. Soc. Rev. 48 (2019) 4979–5015, https://doi.org/10.1039/c8cs00997j.

[8] Y. Miao, M. Shao, Photoelectrocatalysis for high-value-added chemicals production, Chin. J. Catal. 43 (2022) 595–610, https://doi.org/10.1016/S1872-2067(21)63923-2.

[9] B. Zhang, S. Yu, Y. Dai, X. Huang, L. Chou, G. Lu, G. Dong, Y. Bi, Nitrogen-incorporation activates NiFeOx catalysts for efficiently boosting oxygen evolution activity and stability of BiVO4 photoanodes, Nat. Commun. 12 (2021) 6969, https://doi.org/10.1038/s41467-021-27299-0.

[10] Y. Song, X. Zhang, Y. Zhang, P. Zhai, Z. Li, D. Jin, J. Cao, C. Wang, B. Zhang, J. Gao, L. Sun, J. Hou, Engineering MoOx/MXene hole transfer layers for unexpected boosting of photoelectrochemical water oxidation, Angew. Chem. Int. Ed. 61 (2022), e202200946, https://doi.org/10.1002/anie.202200946.

[11] G. Liu, J. Shi, F. Zhang, Z. Chen, J. Han, C. Ding, S. Chen, Z. Wang, H. Han, C. Li, A. Tantalum, Nitride photoanode modified with a hole-storage layer for highly stable solar water splitting, Angew. Chem. Int. Ed. 53 (2014) 7295–7299, https://doi.org/10.1002/anie.201404697.

[12] K. Zhang, B. Jin, C. Park, Y. Cho, X. Song, X. Shi, S. Zhang, W. Kim, H. Zeng, J. H. Park, Black phosphorene as a hole extraction layer boosting solar water splitting of oxygen evolution catalysts, Nat. Commun. 10 (2019) 2001, https://doi.org/10.1038/s41467-019-10034-1.

[13] Z. Yu, H. Liu, M. Zhu, Y. Li, W. Li, Interfacial charge transport in 1D TiO2 based photoelectrodes for photoelectrochemical water splitting, Small 17 (2021) 1903378, https://doi.org/10.1002/smll.201903378.

[14] S. Byun, B. Kim, S. Jeon, B. Shin, Effects of a SnO2 hole blocking layer in a BiVO4-based photoanode on photoelectrocatalytic water oxidation, J. Mater. Chem. A 5 (2017) 6905–6913, https://doi.org/10.1039/c7ta00806f.

[15] Z. Wang, X. Mao, P. Chen, M. Xiao, S.A. Monny, S. Wang, M. Konarova, A. Du, L. Wang, Understanding the roles of oxygen vacancies in hematite-based photoelectrochemical processes, Angew. Chem. Int. Ed. 58 (2019) 1030–1034, https://doi.org/10.1002/anie.201810583.

[16] D. Chen, Z. Liu, S. Zhang, Enhanced PEC performance of hematite photoanode coupled with bimetallic oxyhydroxide NiFeOOH through a simple electroless method, Appl. Catal. B Environ. 265 (2020), 118580, https://doi.org/10.1016/j.apcatb.2019.118580.

[17] D. Wang, T. Sheng, J. Chen, H. Wang, P. Hu, Identifying the key obstacle in photocatalytic oxygen evolution on rutile TiO2, Nat. Catal. 1 (2018) 291–299, https://doi.org/10.1038/s41929-018-0055-z.

[18] C.R. Lhermitte, K. Sivula, Alternative oxidation reactions for solar-driven fuel production, ACS Catal. 9 (2019) 2007–2017, https://doi.org/10.1021/acscatal.8b04565.

[19] R. Zhang, M. Shao, Z. Li, F. Ning, M. Wei, D.G. Evans, X. Duan, Photoelectrochemical catalysis toward selective anaerobic oxidation of alcohols, Chem. Eur. J. 23 (2017) 8142–8147, https://doi.org/10.1002/chem.201701107.

[20] C.A. Mesa, A. Kafizas, L. Francàs, S.R. Pendlebury, E. Pastor, Y. Ma, F. Le Formal, M.T. Mayer, M. Grätzel, J.R. Durrant, Kinetics of photoelectrochemical oxidation of methanol on hematite photoanodes, J. Am. Chem. Soc. 139 (2017) 11537–11543, https://doi.org/10.1021/jacs.7b05184.

[21] N. Karjule, R.S. Phatake, S. Barzilai, B. Mondal, A. Azoulay, A.I. Shames, M. Volokh, J. Albero, H. García, M. Shalom, Photoelectrochemical alcohols oxidation over polymeric carbon nitride photoanodes with simultaneous H2

production, J. Mater. Chem. A 10 (2022) 16585–16594, https://doi.org/10.1039/d2ta03660f.

[22] H.G. Cha, K.S. Choi, Combined biomass valorization and hydrogen production in a photoelectrochemical cell, Nat. Chem. 7 (2015) 328–333, https://doi.org/10.1038/nchem.2194.

[23] Y. Liu, M. Wang, B. Zhang, D. Yan, X. Xiang, Mediating the oxidizing capability of surface-bound hydroxyl radicals produced by photoelectrochemical water oxidation to convert glycerol into dihydroxyacetone, ACS Catal. 12 (2022) 6946–6957, https://doi.org/10.1021/acscatal.2c01319.

[24] T. Li, T. Kasahara, J. He, K.E. Dettelbach, G.M. Sammis, C.P. Berlinguette, Photoelectrochemical oxidation of organic substrates in organic media, Nat. Commun. 8 (2017) 390, https://doi.org/10.1038/s41467-017-00420-y.

[25] Y. Song, Z. Li, K. Fan, Z. Ren, W. Xie, Y. Yang, M. Shao, M. Wei, Ultrathin layered double hydroxides nanosheets array towards efficient electrooxidation of 5-hydroxymethylfurfural coupled with hydrogen generation, Appl. Catal. B Environ. 299 (2021), 120669, https://doi.org/10.1016/j.apcatb.2021.120669.

[26] C.R. Kao, A.H. Yeh, B.H. Chen, L.M. Lyu, Y.C. Chuang, B.T. Sneed, C.H. Kuo, Insights into transformation of icosahedral PdRu nanocrystals into lattice-expanded nanoframes with strain enhancement in electrochemical redox reactions, Chem. Mater. 34 (2022) 2282–2291, https://doi.org/10.1021/acs.chemmater.1c04093.

[27] S. Li, R. Ma, J. Hu, Z. Li, L. Liu, X. Wang, Y. Lu, G.E. Sterbinsky, S. Liu, L. Zheng, J. Liu, D. Liu, J. Wang, Coordination environment tuning of nickel sites by oxyanions to optimize methanol electro-oxidation activity, Nat. Commun. 13 (2022) 2916, https://doi.org/10.1038/s41467-022-30670-4.

[28] D. Kang, Y. Park, J.C. Hill, K.-S. Choi, Preparation of Bi-based ternary oxide photoanodes BiVO$_4$, Bi$_2$WO$_6$, and Bi$_2$Mo$_3$O$_{12}$ using dendritic Bi metal electrodes, J. Phys. Chem. Lett. 5 (2014) 2994–2999, https://doi.org/10.1021/jz501544k.

[29] Y. Zuo, Y. Liu, J. Li, R. Du, X. Yu, C. Xing, T. Zhang, L. Yao, J. Arbiol, J. Llorca, K. Sivula, N. Guijarro, A. Cabot, Solution-processed ultrathin SnS$_2$–Pt nanoplates for photoelectrochemical water oxidation, ACS Appl. Mater. Interfaces 11 (2019) 6918–6926, https://doi.org/10.1021/acsami.8b17622.

[30] T. Boningari, P.R. Ettireddy, A. Somogyvari, Y. Liu, A. Vorontsov, C.A. Mcdonald, P.G. Smirniotis, Influence of elevated surface texture hydrated titania on Ce-doped Mn/TiO$_2$ catalysts for the low-temperature SCR of NO$_x$ under oxygen-rich conditions, J. Catal. 325 (2015) 145–155, https://doi.org/10.1016/j.jcat.2015.03.002.

[31] Z. Li, X. Zhang, Y. Kang, C.C. Yu, Y. Wen, M. Hu, D. Meng, W. Song, Y. Yang, Interface engineering of Co-LDH@MOF heterojunction in highly stable and efficient oxygen evolution reaction, Adv. Sci. 8 (2021) 2002631, https://doi.org/10.1002/advs.202002631.

[32] S. Zhou, K. Chen, J. Huang, L. Wang, M. Zhang, B. Bai, H. Liu, Q. Wang, Preparation of heterometallic CoNi-MOFs-modified BiVO$_4$: a steady photoanode for improved performance in photoelectrochemical water splitting, Appl. Catal. B Environ. 266 (2020), 118513, https://doi.org/10.1016/j.apcatb.2019.118513.

[33] Z. Li, K. Liu, K. Fan, Y. Yang, M. Shao, M. Wei, X. Duan, Active-oxygen-enhanced homogeneous nucleation of lithium metal on ultrathin layered double hydroxide, Angew. Chem. 131 (2019) 4002–4006, https://doi.org/10.1002/ange.201814705.

[34] W. Qiao, B. Jin, W. Xie, M. Shao, M. Wei, Hierarchical CoNi-LDH nanosheet array with hydrogen vacancy for high-performance aqueous battery cathode, J. Energy Chem. 69 (2022) 9–15, https://doi.org/10.1016/j.jechem.2021.09.012.

[35] M.N. Shaddad, M.A. Ghanem, A.M. Al-mayouf, S. Gimenez, J. Bisquert, I. Herraiz-Cardona, Cooperative catalytic effect of ZrO$_2$ and α-Fe$_2$O$_3$ nanoparticles on BiVO$_4$ photoanodes for enhanced photoelectrochemical water splitting, ChemSusChem 9 (2016) 2779–2783, https://doi.org/10.1002/cssc.201600890.

[36] S. Wang, P. Chen, J.H. Yun, Y. Hu, L. Wang, An electrochemically treated BiVO$_4$ photoanode for efficient photoelectrochemical water splitting, Angew. Chem. Int. Ed. 56 (2017) 8500–8504, https://doi.org/10.1002/anie.201703491.

[37] P. Babu, H. Kim, J.Y. Park, B. Naik, Trioctylphosphine oxide (TOPO)-assisted facile fabrication of phosphorus-incorporated nanostructured carbon nitride toward photoelectrochemical water splitting with enhanced activity, Inorg. Chem. 61 (2022) 1368–1376, https://doi.org/10.1021/acs.inorgchem.1c02863.

[38] H. Wang, Y. Xia, H. Li, X. Wang, Y. Yu, X. Jiao, D. Chen, Highly active deficient ternary sulfide photoanode for photoelectrochemical water splitting, Nat. Commun. 11 (2020) 3078, https://doi.org/10.1038/s41467-020-16800-w.

[39] Z.Q. Wei, S. Hou, X. Lin, S. Xu, X.C. Dai, Y.H. Li, J.Y. Li, F.X. Xiao, Y.J. Xu, Unexpected boosted solar water oxidation by nonconjugated polymer-mediated tandem charge transfer, J. Am. Chem. Soc. 142 (2020) 21899–21912, https://doi.org/10.1021/jacs.0c11057.

[40] M. Shi, H. Zhou, W. Tian, B. Yang, S. Yang, K. Han, R. Li, C. Li, Lead-free B-site bimetallic perovskite photocatalyst for efficient benzylic C–H bond activation, Cell Rep. Phys. Sci. 2 (2021), 100656, https://doi.org/10.1016/j.xcrp.2021.100656.

[41] J. Cai, B. Niu, H. Zhao, G. Zhao, Selective photoelectrocatalytic removal for group-targets of phthalic esters, Environ. Sci. Technol. 55 (2021) 2618–2627, https://doi.org/10.1021/acs.est.0c07106.

[42] J. Zhang, Y. Nosaka, Mechanism of the OH radical generation in photocatalysis with TiO$_2$ of different crystalline types, J. Phys. Chem. C 118 (2014) 10824–10832, https://doi.org/10.1021/jp501214m.

[43] T. Jedsukontorn, V. Meeyoo, N. Saito, M. Hunsom, Effect of electron acceptors H$_2$O$_2$ and O$_2$ on the generated reactive oxygen species ^{1}O$_2$ and OH$^-$ in TiO$_2$-catalyzed photocatalytic oxidation of glycerol, Chin. J. Catal. 37 (2016) 1975–1981, https://doi.org/10.1016/S1872-2067(16)62519-6.

[44] L. Luo, W. Chen, S.M. Xu, J. Yang, M. Li, H. Zhou, M. Xu, M. Shao, X. Kong, Z. Li, H. Duan, Selective photoelectrocatalytic glycerol oxidation to dihydroxyacetone via enhanced middle hydroxyl adsorption over a Bi$_2$O$_3$-incorporated catalyst, J. Am. Chem. Soc. 144 (2022) 7720–7730, https://doi.org/10.1021/jacs.2c00465.

[45] D. Liu, J.C. Liu, W. Cai, J. Ma, H. Bin Yang, H. Xiao, J. Li, Y. Xiong, Y. Huang, B. Liu, Selective photoelectrochemical oxidation of glycerol to high value-added dihydroxyacetone, Nat. Commun. 10 (2019) 1779, https://doi.org/10.1038/s41467-019-09788-5.